Bone Adaptation as Level Set Motion

Bryce A. Besler[1,2,4(✉)], Leigh Gabel[2,4], Lauren A. Burt[2,4], Nils D. Forkert[3,4], and Steven K. Boyd[2,4]

[1] Biomedical Engineering Graduate Program, University of Calgary, Calgary, Canada
babesler@ucalgary.ca
[2] McCaig Institute for Bone and Joint Health, University of Calgary, Calgary, Canada
[3] Hotchkiss Brain Institute, University of Calgary, Calgary, Canada
[4] Department of Radiology, Cumming School of Medicine, University of Calgary, Calgary, Canada

Abstract. Bone microarchitecture is constantly adapting to environmental and mechanical factors. Changes in bone density and structure can lead to an increase in fracture risk. Computational modeling of bone adaptation may provide insight into mitigating aging and preventing disease. In this paper, the adaptation of bone is modeled as a curve evolution problem. Curves can be evolved according to the level set method. The level set method models basic bone physiology by adapting bone according to appositional growth following a trajectory in time with a natural definition of homeostasis. A novel curvature based bone adaptation algorithm is presented for modeling bone atrophy. The algorithm is shown to be weakly equivalent to simulated bone atrophy. These results generalize surface-driven and strain-driven models of bone adaptation using a surface remodeling force. Physiological signals (hormones, mechanical strain, etc.) can be directly integrated into this surface remodeling force. Remodeling can be naturally restricted around foreign bodies (such as modeling adaptation around a surgical screw). Future work aims to identify the surface remodeling force from longitudinal image data.

Keywords: Level set method · Bone adaptation · Cancellous bone
Finite difference method

1 Introduction

Bone is a dynamic organ changing shape and density in time. Constantly, bone is undergoing a process of remodeling, where cellular processes remove old bone and lay down new bone [1]. Bone adaptation is driven by many factors, including genetics, hormones, and mechanical loading [2]. An imbalance in resorption and formation can lead to a degradation of bone microarchitecture, increasing the risk of fracture. Computational modeling of bone adaptation can provide insight into aging and metabolic bone diseases such as osteoporosis.

T. Vrtovec et al. (Eds.): MSKI 2018, LNCS 11404, pp. 58–72, 2019.
https://doi.org/10.1007/978-3-030-11166-3_6

In this paper, the physiological process of bone adaptation is modeled using level set motion. In Sect. 2, a framework is presented for modeling bone adaptation as a curve evolution problem. Bone physiology and curve evolution are reviewed and used to derive a surface-only model of bone atrophy based on mean curvature and advection. In Sect. 3, numerical techniques for solving the partial differential equation are summarized. In Sect. 4, quadratic surfaces are used to demonstrate that the algorithm produces physiologically plausible changes. Finally, in Sect. 5, curvature based bone adaptation is shown to generalize a classic surface-driven model of bone atrophy using *in vivo* image data.

2 Bone Adaptation as Level Set Motion

Cancellous bone is a mixture of marrow tissue and trabeculae tissue. Bone can only remodel at the surface – so-called appositional growth [1]. The interface between marrow tissue and trabeculae tissue defines a surface. Remodeling of bone microarchitecture can be conceptualized as an evolution of this surface.

2.1 Bone Microarchitecture as a Curve

First, the trabecular surface is modeled by a planar curve $\mathcal{C}$, which maps the normalized length along the curve to a two-dimensional coordinate:

$$\mathcal{C} : [0, 1] \rightarrow \mathbb{R}^2. \tag{1}$$

The curve requires an explicit parameterization, which is typically realized using splines [3]. The curve can be evolved in time along its normal vector $\boldsymbol{N}$ according to a force F:

$$\mathcal{C}_t = F\boldsymbol{N}, \tag{2}$$

where $\mathcal{C}_t$ is the time derivative of the curve. Importantly, the force F can depend on mean curvature, κ. This definition of a curve is inherently limited to planar curves. Furthermore, parameterized curves cannot change topology without explicit breaking and merging rules.

Alternatively, a curve can be defined as the level set of an embedding function [4]. Let ϕ be an N-dimensional image defined on domain $\Omega \in \mathbb{Z}^n$ and map each point $x \in \Omega$ to $\mathbb{R}$. The curve $\mathcal{C}$ is defined as the zero level set of the embedding function ϕ:

$$\mathcal{C} = \{x | x \in \Omega, \phi(x) = 0\}. \tag{3}$$

The level set may be evolved by some force, F, by noting that (3) must hold for all time [5]:

$$\phi\left(\mathcal{C}(t), t\right) = 0. \tag{4}$$

By differentiating (4) with respect to time, the following equation of motion for N-dimensional curves is found:

$$\phi_t + F|\nabla\phi| = 0. \tag{5}$$

Similar to (2), the force F may depend on mean curvature, κ. Curvature can be computed directly from the embedding image ϕ as the divergence of the normal vectors to the curve [6]:

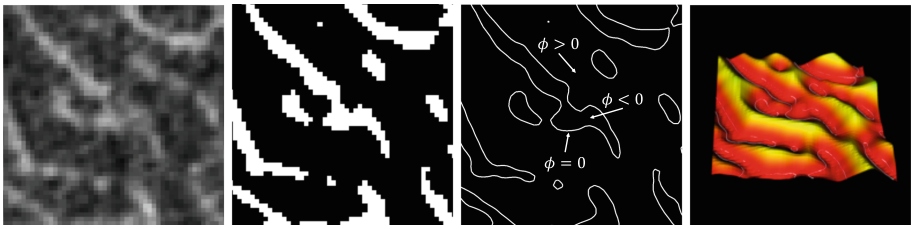

(a) Hounsfield Units (b) Segmentation (c) Contour (d) Surface

Fig. 1. Embedding computed tomography data in a level set. Although a two-dimensional image is shown, the embedding is done on three-dimensional data.

$$\kappa = \nabla \cdot \boldsymbol{N}, \tag{6}$$

$$\kappa = \nabla \cdot \left(\frac{\nabla \phi}{|\nabla \phi|} \right). \tag{7}$$

There are many possible choices of ϕ. Here, ϕ is defined as the signed distance between a voxel and the curve:

$$\phi(x) = \pm d\left(x, \mathcal{C}\right). \tag{8}$$

The distance $\pm d\left(x, \mathcal{C}\right)$ is a signed Euclidean distance such that $d < 0$ is inside the curve and $d > 0$ is outside the curve. The image ϕ can be computed in linear time from a binarized image of cancellous bone [7]. Figure 1 demonstrates the concept of embedding trabecular bone in a level set.

The level set formulation of curve evolution has many advantages. First, the definition is non-parametric. More precisely, the curve is implicitly parameterized by the domain of the image instead of relying on a parameterization such as splines. Second, the level set method implicitly handles changes in topology. This is important for modeling the resorption of trabecular bone because thin trabecular rods can completely resorb, changing the topology of the bone [8].

2.2 Functional Adaptation as Curve Evolution

Functional bone adaptation is defined as the ability of bone to form or resorb according to local mechanical strain [9]. The curve force F of functional bone adaptation is a surface remodeling rate modulated by local physiological signals (e.g. mechanical strain, hormones, etc.) [2]. Micro-computed tomography can resolve individual trabeculae (on the order of 100 µm) in three dimensions (3D) enabling visualization and quantification of bone adaptation [10,11]. The

cancellous bone can be binarized using a density threshold on the computed tomography data. Using finite element modeling [12] with an assumed loading condition, strain energy density can be computed at each voxel. Relating strain energy density to surface remodeling rate gives the curve force F in (5) [13]. Although finite element modeling is not performed in the following experiments, it is important to recognize that the level set method is a general framework for modeling strain- and surface-based bone adaptation.

Importantly, these models present bone adaptation as an initial value problem:

$$\begin{cases} \dfrac{\partial \phi(x,t)}{\partial t} = -F|\nabla \phi(x,t)|, \\ \phi(x,0) = \phi_0(x). \end{cases} \tag{9}$$

The initial value problem implies that bone adapts according to a trajectory in time. Knowing the state of the bone at time t_0 and knowledge of how bone functionally adapts (by force F at the surface), a unique solution can be found for all t. Furthermore, the curve stops updating when the force F goes to zero (that is, $\phi_t = 0$). This implies a state of homeostasis, important for modeling metabolic diseases such as osteoporosis [14]. The surface remodeling rate F is the fundamental measure needed to understand functional bone adaptation [15–17].

2.3 Bone Adaptation by Advection and Mean Curvature

Surface-based models of bone adaptation are important for understanding longitudinal changes in trabecular bone. One such model was simulated bone atrophy (SIBA) [8], where one iteration of the remodeling cycle was simulated at a time. The basis of this approach was that bone remodeling occurs in discrete packets termed Basic Multicellular Units (BMUs). In one remodeling cycle, a BMU is recruited, osteoclast cells resorb bone mineral, and osteblast cells replace this bone in a sequential fashion [1]. Given a binary image of bone, SIBA simulates one remodeling cycle using a Gaussian blur, where a finite impulse response Gaussian filter smooths the edges of the binary image data producing a greyscale image. Subsequently applying a threshold, the greyscale data could be re-binarized. The Gaussian filter standard deviation and support were chosen on the basis of osteoclast penetration depth. The threshold was chosen based on osteoblast efficiency, or percentage of bone resorbed by osteoclasts that osteoblasts replaced, and the time between iterations was chosen as the activation frequency of BMUs. SIBA can be viewed as a net advection and curvature-based loss when a threshold less than 50% is chosen and Gaussian smoothing is included. The approach we present reframes SIBA in the level set motion framework. This is a novel method for modeling age-related bone loss, and importantly unifies surface-based and strain-based models of bone adaptation.

As in Sect. 2.1, consider a curve, $\mathcal{C}$, defining the marrow-trabecular interface. To model appositional growth, one seeks to adapt this curve in time by some force F in the direction of the normal to the curve:

$$\mathcal{C}_t = F\boldsymbol{N}. \tag{10}$$

In 3D, the curve can be seen as the level set of an embedding function ϕ. An equation of motion for the curve can be found:

$$\phi_t + F|\nabla\phi| = 0. \tag{11}$$

The force is chosen to have an advection and curvature loss:

$$F = a - b\kappa. \tag{12}$$

By selecting a positive, the curve will grow, increasing the trabecular bone volume. Conversely, negative a causes the curve to shrink, decreasing the trabecular bone volume. The curvature term is only well-posed for b positive [6]. a is measured in units of μm/year and b is measured in units of μm^2/year. Combining (11) and (12), an equation of motion for the trabecular bone surface can be found:

$$\phi_t = b\kappa|\nabla\phi| - a|\nabla\phi|. \tag{13}$$

Finally, the curve evolution problem can be formulated as an initial value problem by taking $\phi_0(x)$ as the signed Euclidean distance transform of binarized computed tomography data:

$$\begin{cases} \dfrac{\partial\phi(x,t)}{\partial t} = b\kappa|\nabla\phi(x,t)| - a|\nabla\phi(x,t)|, \\ \phi(x,0) = \phi_0(x). \end{cases} \tag{14}$$

Most importantly, the parameters a and b must be selected to represent physiologically plausible change. As with SIBA, the majority of the loss should be accounted for by mean curvature [8]. For this reason, $b\kappa$ should be chosen on the same order or larger in magnitude than a. Average loss may provide some insight into the absolute scale of the parameters. For idealized cylindrical rods, the mean curvature is known to be the inverse of twice the radius. Using this, an equation for surface remodeling rate l given a cylinder of radius r can be found:

$$l(r) = a - b\kappa = a - \frac{b}{2r}. \tag{15}$$

Equation (15) is plotted in Fig. 2. Graphically, Fig. 2 demonstrates that the surface remodeling rate accelerates with time for rod-like structures. The mean thickness of trabecular bone ranges from 150 μm to 250 μm [18]. Using this model and knowledge of thickness, the following parameters were selected: $a = -1\,\mu$m/year, $b = 100\,\mu m^2$/year. This gives a loss of $-1.5\,\mu$m/year for a 100 μm rod. Note that after one year, the radius decreases and the rate increases in accordance with (15) and Fig. 2. This leads to a cascading loss.

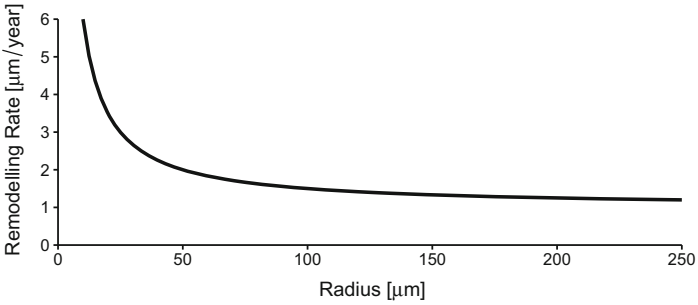

Fig. 2. Plot of surface remodeling rate as a function of radius for a rod-like structure ($a = -1\,\mu\text{m/year}$, $b = 10\,\mu\text{m}^2/\text{year}$).

Algorithm 1. Curvature Based Bone Adaptation

Require: ϕ_0, a, $b > 0$, $t > 0$
$\phi = \phi_0$
elapsed $= 0$
while elapsed $< t$ **do**
  ϕ = Reinitialize(ϕ)
  dt = min (t - elapsed, TimeStep(a,b,ϕ))
  for all $x \in \Omega$ **do**
    update = b CurvatureTerm($\phi(x)$) - a AdvectionTerm(a, $\phi(x)$)
    $\phi(x) = \phi(x)$+ dt $\cdot$ update
  end for
  elapsed += dt
end while
return ϕ

3 Numerical Implementation

The finite difference method is employed to numerically solve (14). Time and space discretization are described in detail below. Since trabecular bone surface is dense in the image domain, narrow band methods are not employed [6]. The algorithm takes an initial distance transform ϕ_0, the advection and mean curvature weights a and b, and a total time to iterate t and returns the final embedded level set. A multithreaded implementation written in C++ and based on The Insight Segmentation and Registration Toolkit[1] is available online[2]. The program is summarized in Algorithm 1. In the following sections, the algorithm is applied to idealized surfaces and *in vivo* image data.

[1] www.itk.org.
[2] https://github.com/Bonelab/Bone_Adaptation_as_Level_Set_Motion.

3.1 Time Discretization

The forward Euler method can be used for time discretization. However, the spatial discretization of mean curvature and advection require special care [4]:

$$\phi(x, t + \Delta t) = \phi(x, t) + \Delta t \left[b\kappa |\nabla \phi(x, t)| - a|\nabla \phi(x, t)| \right]. \tag{16}$$

3.2 Advection Term

The advection term will be spatially discretized using the upwind scheme [4]. Let $\phi_i \equiv \frac{\partial \phi(x,t)}{\partial x_i}$ denote the derivative of ϕ with respect to direction x_i. The gradient magnitude can be written as such:

$$|\nabla \phi(x, t)| = \sqrt{\sum_i \phi_i^2}. \tag{17}$$

An upwind finite difference method is used to compute the first order partial derivatives. This is done by calculating the derivative on the edge to which the wave moves. This scheme is known to capture shocks in the evolving wave front. First, forward edge and backwards edge derivative operators are defined:

$$D_i^+ \phi = \frac{\phi_{i+1,j,k} - \phi_{i,j,k}}{\Delta x_i}, \tag{18}$$

$$D_i^- \phi = \frac{\phi_{i,j,k} - \phi_{i-1,j,k}}{\Delta x_i}. \tag{19}$$

The squared partial derivative is estimated by taking into account the direction of wave propagation:

$$\phi_i^2 = \begin{cases} \max\left(D_i^- \phi, 0\right)^2 + \min\left(D_i^+ \phi, 0\right)^2, & \text{if } a \geq 0, \\ \min\left(D_i^- \phi, 0\right)^2 + \max\left(D_i^+ \phi, 0\right)^2, & \text{if } a < 0. \end{cases} \tag{20}$$

3.3 Curvature Term

The curvature term is spatially discretized using central differences [6]. The curvature can be calculated from the level set as the divergence of the normal:

$$\kappa = \nabla \cdot \boldsymbol{N}, \tag{21}$$

$$\kappa = \nabla \cdot \left(\frac{\nabla \phi}{|\nabla \phi|} \right), \tag{22}$$

$$\kappa = \frac{\triangle \phi}{|\nabla \phi|} - \frac{1}{|\nabla \phi|^3} \sum_i \sum_j \phi_i \phi_j \phi_{ij}, \tag{23}$$

where $\triangle \phi = \nabla \cdot \nabla \phi$ denotes the Laplacian of ϕ and $\phi_{i,j} \equiv \frac{\partial^2 \phi(x,t)}{\partial x_i \partial x_j}$ denotes the second derivative of ϕ with respect to x_i, x_j. Using (23) and assuming ϕ has

continuous derivatives such that $\phi_{ij} = \phi_{ji}$, the mean curvature term can then be reduced to the following:

$$\kappa|\nabla\phi(x,t)| = |\nabla\phi| \left(\frac{\triangle\phi}{|\nabla\phi|} - \frac{1}{|\nabla\phi|^3} \sum_i \sum_j \phi_i \phi_j \phi_{ij} \right), \tag{24}$$

$$\kappa|\nabla\phi(x,t)| = \frac{1}{|\nabla\phi|^2} \left(\sum_i \phi_i^2 \sum_{j \neq i} \phi_{jj} - 2 \sum_i \sum_{j=i+1} \phi_i \phi_j \phi_{ij} \right). \tag{25}$$

The derivatives in (25) are discretized using central differences since the value depends on cross derivatives in different spatial directions [6]:

$$\phi_i = \frac{\phi_{i+1,j,k} - \phi_{i-1,j,k}}{2\Delta x_i}, \tag{26}$$

$$\phi_{ij} = \begin{cases} \frac{\phi_{i+1,j,k} - 2\phi_{i,j,k} + \phi_{i-1,j,k}}{(\Delta x_i)^2}, \text{if } i = j, \\ \frac{\phi_{i+1,j+1,k} - \phi_{i-1,j+1,k} - \phi_{i+1,j-1,k} + \phi_{i-1,j-1,k}}{4\Delta x_i \Delta x_j}, \text{if } i \neq j. \end{cases} \tag{27}$$

3.4 Courant-Friedrichs-Lewy Condition

The level set method provides a strong numerical basis for choosing time steps based on the speed of curve evolution relative to image spacing. The so-called Courant-Friedrichs-Lewy (CFL) condition requires that the numerical domain of dependence includes the analytic domain of dependence [19]. Using an upwind finite difference for the advection term and central differences for the mean curvature term, the following CFL condition must be met for each voxel [6]:

$$\alpha = \Delta t \left(\frac{|a|}{\min\{\Delta x, \Delta y, \Delta z\}} + \frac{2|b|}{\min\{(\Delta x)^2, (\Delta y)^2, (\Delta z)^2\}} \right) < 1. \tag{28}$$

For these experiments, the CFL number was set to a conservative $\alpha = 0.5$ [6].

3.5 Reinitialization

Finally, introduction of a mean curvature term with forward Euler time discretization can cause ϕ to deviate from a signed distance function. Periodically, reinitialization is needed to return the level set to a signed distance function [6]. The technique used here solves the following reinitialization equation [20]:

$$\phi_t + S(\phi)(|\nabla\phi| - 1) = 0, \tag{29}$$

$$S(\phi) = \frac{\phi}{\sqrt{\phi^2 + |\nabla\phi|^2 \epsilon^2}}, \tag{30}$$

where $\epsilon = \min\{\Delta x, \Delta y, \Delta z\}$. Reinitialization updates the embedding function to maintain the property that for a signed distance function, $|\nabla\phi| = 1$. The term $S(\phi)$ is the regularized sign of the embedding function.

4 Quadratic Surfaces

To gain insight into the correctness of the resorption algorithm, simple representations of rods and plates will be created using quadratic surfaces. The implicit function of a quadratic surface can be used to instantiate an idealized rod or plate in image data. Below, quadratic surfaces are defined according to physical properties of a rod or plate. The instantiated image data can be created with varying image resolutions, but will not be explored here.

4.1 Cylindrical Rod

A rod of constant thickness can be modeled as a cylinder of radius r. This rod will have some length l, which clips the implicit function:

$$x^2 + y^2 - r^2 = 0. \tag{31}$$

4.2 Resorbing Rod

A rod thinning in the center can be modeled as a one sheet hyperbola:

$$b^2x^2 + b^2y^2 - a^2z^2 = 1. \tag{32}$$

The equation is determined by three parameters: the length of the rod, l; the radius at the ends of the rod, R; and the radius at the center of the rod, r:

$$a = \frac{2}{l}\sqrt{\frac{R^2}{r^2} - 1}, \tag{33}$$

$$b = \frac{1}{r}. \tag{34}$$

4.3 Resorbing Plate

Finally, a plate can be modeled as a torus. Given below is the equation of a torus:

$$\left(\sqrt{x^2 + y^2} - R\right)^2 + a^2z^2 = r^2. \tag{35}$$

By varying R with respect to r, the size of the hole through the torus can be controlled. If $r > R$, the hole can be closed.

The equation of the torus is determined by three parameters: the diameter of the plate, l; the resorption distance, d; and the plate thickness, t:

$$r = \frac{l - d}{4}, \tag{36}$$

$$R = \frac{l + d}{4}, \tag{37}$$

$$a = \frac{l - d}{2t}. \tag{38}$$

If the resorption distance is negative, the hole in the torus will be closed.

4.4 Proof-of-Principle

Three surfaces are generated to visualize the curvature based bone adaptation algorithm. The cases are outlined in Fig. 3. For each case, the implicit functions above are used to generate a representation of the surface in a binary image. The spacing of the images are set to an isotropic resolution of 61 μm. Fifty years of aging are simulated using the parameters $a = -1\,\mu\text{m/year}$ and $b = 100\,\mu\text{m}^2/\text{year}$. The surfaces are visualized directly from the embedding function ϕ using the Marching Cubes algorithm [21].

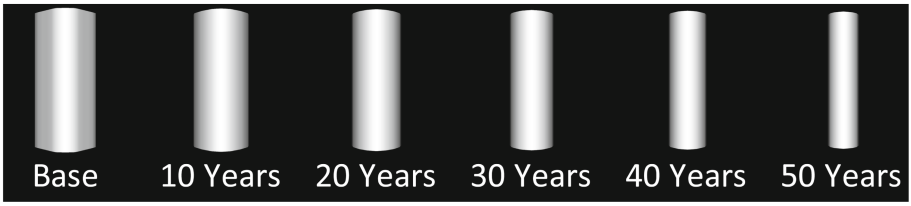

(a)

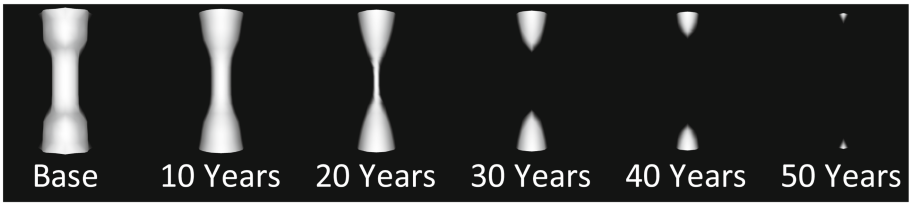

(b)

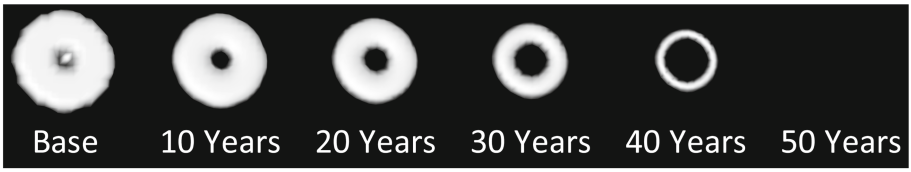

(c)

Fig. 3. Plot of ideal structures adapting in time. Three cases are demonstrated: (a) Cylindrical rod ($l = 1\,\text{mm}$, $r = 200\,\mu\text{m}$). (b) Resorbing rod ($l = 1\,\text{mm}$, $R = 200\,\mu\text{m}$, $r = 100\,\text{mm}$). (c) Resorbing plate ($l = 1\,\text{mm}$, $d = 100\,\text{mm}$, $t = 200\,\text{mm}$).

Many important features of the algorithm are demonstrated in Fig. 3. The resorbing rod (Fig. 3(b)) and plate (Fig. 3(c)) are completely removed while the cylindrical rod (Fig. 3(a)) thins. This agrees with the intuition behind (15) and Fig. 2 that higher curvature structures resorb faster. Additionally, the topological change in the resorbing rod is handled implicitly. Handling topolgical changes is a critical feature for any algorithm modeling bone adaptation. Finally, the resorbing plate reduces to a ring. Both the outer and inner portions of the ring

resorb. Curvature based bone adaptation demonstrates physiologically plausible changes to idealized rods and plates.

5 *In vivo* Experiments

5.1 Data Collection

Curvature based bone adaptation is applied to *in vivo* human data as a model of aging. The left, distal tibia of ten subjects were imaged using second generation high-resolution peripheral quantitative computed tomography (HR-pQCT; XtremeCT II, SCANCO Medical AG, Switzerland). Second generation HR-pQCT is capable of directly assessing human trabecular bone [18]. The nominal resolution was 61 µm isotropic. 50% (5) of the subjects were female. Age ranged from 56 to 67 years. Total bone mineral density ranged from 279.6 mg HA/ccm to 317.5 mg HA/ccm. Age- and sex-matched normative total bone mineral density ranged from 48.3% to 53.5% [22].

5.2 Pre-processing

Cortical and cancellous masks for each tibia volume were generated using the dual thresholding technique [23]. Masks were visually inspected and manually corrected. Image data was binarized using a threshold of 320 mg HA/ccm.

5.3 Simulation

For each subject, 30 years of bone loss was simulated. The simulation parameters were unchanged ($a = -1\,\mu\text{m/year}$, $b = 100\,\mu\text{m}^2\text{/year}$). However, a mask of the trabecular bone was included to restrict the remodeling force F to the trabecular region. Outside the trabecular mask, F was set to zero. Image data was generated at every decade, and bone volume fraction in the cancellous compartment was quantified. Additionally, the bone surface area to volume ratio was quantified for the measured data. The surface area to volume ratio is a measure of the shape of the trabecular bone and is a strong determinant of bone loss in SIBA [8]. The surfaces were visualized directly from the embedding function ϕ using the Marching Cubes algorithm [21].

5.4 Results

The change in morphometry with simulated aging is analyzed. A plot of trabecular bone volume fraction with simulated age is shown in Fig. 4(a). Each subject experiences monotonic bone loss with age. Subjects appear to lose bone at the same absolute rate. This can be explained by having selecting the same parameters (a and b) for each subject. Figure 4(b) shows the percent bone loss over 30 years as a function of original bone surface to volume ratio. 99% of the variation in lost bone volume fraction is explained by the original bone surface

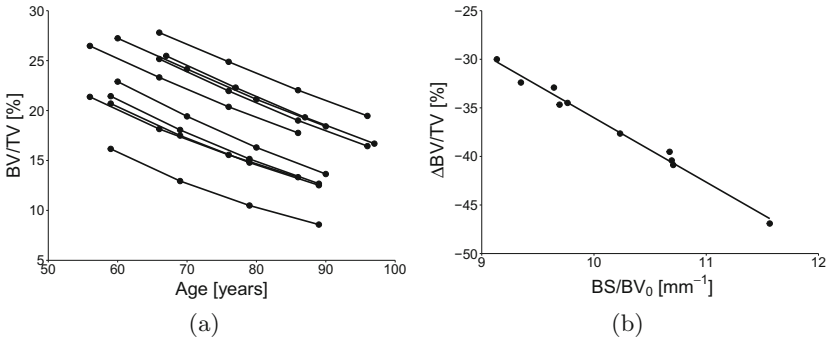

Fig. 4. Change in bone morphometry with simulated age. (a) Trabecular bone volume fraction decreases with simulated age for ten subjects. (b) Original bone surface to bone volume ratio predicts percentage bone loss ($R^2 = 0.99$).

to volume ratio ($p < 0.05$). This is a key finding in the original work on SIBA [8]. Curvature loss for one subject is shown in Figs. 5 and 6. The subject is a 60 year old male with an original bone volume fraction of 22.9% and a bone surface to volume ratio of 10.7 mm^{-1}. No loss is seen in the cortical bone where the curve force was set to zero. This is an important feature for modeling complex interactions such as adaptation around a surgical screw. Qualitatively, more bone loss is seen in the center of the bone than the endosteal surface (Fig. 5). This loss visually corresponds with a thin, rod-like initial structure. Plates connected by thin trabecular rods can become disconnected, a feature also present in SIBA. Trabeculae disconnect, holes in plates widen, and loss is seen throughout the structure (Fig. 6). Curvature based bone adaptation appears to model the same mechanism of bone loss as the SIBA algorithm.

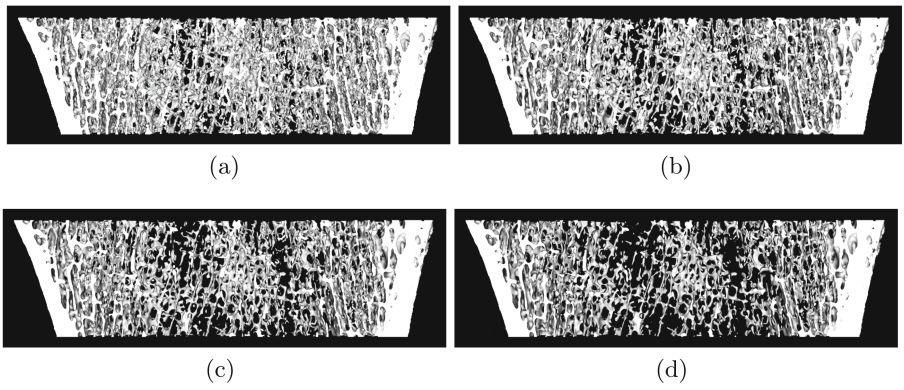

Fig. 5. Change in microarchitecture under curvature based bone adaptation for one subject at (a) baseline, (b) 10 years, (c) 20 years, and (d) 30 years.

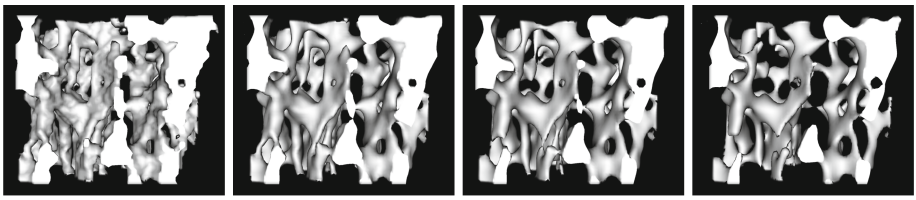

(a) (b) (c) (d)

Fig. 6. Microarchitecture loss visualized for a $49 \times 49 \times 49$ ($26.7\,\mu m^3$) volume for one subject at (a) baseline, (b) 10 years, (c) 20 years, and (d) 30 years.

6 Discussion

In this paper, bone adaptation is presented as level set motion. Functional adaptation is reviewed in the context of level set motion. A new algorithm for curvature based bone adaptation is presented. This algorithm is shown to generalize simulated bone atrophy using level set motion. The algorithm was applied to idealized structures and *in vivo* image data. Level set methods were previously used to model functional bone adaptation. While one study did not explicitly mention level set motion but derived all components [15], the other only mentioned its use in passing [24]. Level set methods have been well characterized. In general, they can be used to model Hamilton-Jacobi type equations from classical mechanics [4]. Traditionally, bone adaptation is presented as an optimization problem where the bone tries to maintain "mechanical competency" while minimizing mass [2]. However, under level set motion, an interesting future area of research is to reframe bone adaptation using principles of least action.

Finally, level set motion presents a general method for adapting the bone surface according to some force. However, identification of the surface force remains elusive [15–17]. Ideally, the motion force F could be determined uniquely given two longitudinal images. This would allow one to uncover the surface remodeling rate of bone directly from the image data. To the best of our knowledge, very little work towards solving the identification problem has been completed [25,26].

7 Conclusion

Level set motion is a general framework for surface-based and strain-based modeling of bone adaptation. The method matches the basic physiology of bone adaptation: appositional growth. A novel algorithm is presented for modeling bone atrophy using mean curvature and advection.

Acknowledgements. B.A. Besler acknowledges support from Alberta Innovates Health Solutions and NSERC CGS-D.

References

1. Clarke, B.: Normal bone anatomy and physiology. Clin. J. Am. Soc. Nephrol. **3**(Suppl. 3), S131–S139 (2008). https://doi.org/10.2215/CJN.04151206
2. Frost, H.: From Wolff's law to the Utah paradigm: insights about bone physiology and its clinical applications. Anat. Rec. **262**(4), 398–419 (2001). https://doi.org/10.1002/ar.1049
3. Kass, M., Witkin, A., Terzopoulos, D.: Snakes: active contour models. Int. J. Comput. Vis. **1**(4), 321–331 (1988). https://doi.org/10.1007/BF00133570
4. Osher, S., Sethian, J.: Fronts propagating with curvature-dependent speed: algorithms based on Hamilton-Jacobi formulations. J. Comput. Phys. **79**(1), 12–49 (1988). https://doi.org/10.1016/0021-9991(88)90002-2
5. Cremers, D., Rousson, M., Deriche, R.: A review of statistical approaches to level set segmentation: integrating color, texture, motion and shape. Int. J. Comput. Vis. **72**(2), 195–215 (2007). https://doi.org/10.1007/s11263-006-8711-1
6. Osher, S., Fedkiw, R.: Level Set Methods and Dynamic Implicit Surfaces. AMS, vol. 153. Springer, New York (2003). https://doi.org/10.1007/b98879
7. Maurer, C., Qi, R., Raghavan, V.: A linear time algorithm for computing exact Euclidean distance transforms of binary images in arbitrary dimensions. IEEE Trans. Pattern Anal. Mach. Intell. **25**(2), 265–270 (2003). https://doi.org/10.1109/TPAMI.2003.1177156
8. Müller, R.: Long-term prediction of three-dimensional bone architecture in simulations of pre-, peri- and post-menopausal microstructural bone remodeling. Osteoporos. Int. **16**(2), S25–S35 (2005). https://doi.org/10.1007/s00198-004-1701-7
9. Ruff, C., Holt, B., Trinkaus, E.: Who's afraid of the big bad Wolff?: "Wolff's law" and bone functional adaptation. Am. J. Phys. Anthropol. **129**(4), 484–498 (2006). https://doi.org/10.1002/ajpa.20371
10. Rüegsegger, P., Koller, B., Müller, R.: A microtomographic system for the nondestructive evaluation of bone architecture. Calcif. Tissue Int. **58**(1), 24–29 (1996). https://doi.org/10.1007/BF02509542
11. Schulte, F., Lambers, F., Kuhn, G., Müller, R.: In vivo micro-computed tomography allows direct three-dimensional quantification of both bone formation and bone resorption parameters using time-lapsed imaging. Bone **48**(3), 433–442 (2011). https://doi.org/10.1016/j.bone.2010.10.007
12. van Rietbergen, B., Weinans, H., Huiskes, R., Odgaard, A.: A new method to determine trabecular bone elastic properties and loading using micromechanical finite-element models. J. Biomech. **28**(1), 69–81 (1995). https://doi.org/10.1016/0021-9290(95)80008-5
13. Schulte, F., et al.: Strain-adaptive in silico modeling of bone adaptation-a computer simulation validated by in vivo micro-computed tomography data. Bone **52**(1), 485–492 (2013). https://doi.org/10.1016/j.bone.2012.09.008
14. Huiskes, R., Ruimerman, R., Van Lenthe, G., Janssen, J.: Effects of mechanical forces on maintenance and adaptation of form in trabecular bone. Nature **405**(6787), 704–706 (2000). https://doi.org/10.1038/35015116
15. Schulte, F., et al.: Local mechanical stimuli regulate bone formation and resorption in mice at the tissue level. PLoS ONE **8**(4), e62172 (2013). https://doi.org/10.1371/journal.pone.0062172
16. Christen, P., et al.: Bone remodelling in humans is load-driven but not lazy. Nat. Commun. **5**, 4855 (2014). https://doi.org/10.1038/ncomms5855

17. Christen, P., Müller, R.: In vivo visualisation and quantification of bone resorption and bone formation from time-lapse imaging. Curr. Osteoporos. Rep. **15**(4), 311–317 (2017). https://doi.org/10.1007/s11914-017-0372-1
18. Manske, S., Zhu, Y., Sandino, C., Boyd, S.: Human trabecular bone microarchitecture can be assessed independently of density with second generation HR-pQCT. Bone **79**, 213–221 (2015). https://doi.org/10.1016/j.bone.2015.06.006
19. Courant, R., Friedrichs, K., Lewy, H.: Über die partiellen Differenzengleichungen der mathematischen Physik. Math. Ann. **100**(1), 32–74 (1928). https://doi.org/10.1007/BF01448839
20. Peng, D., Merriman, B., Osher, S., Zhao, H., Kang, M.: A PDe-based fast local level set method. J. Comput. Phys. **155**(2), 410–438 (1999). https://doi.org/10.1006/jcph.1999.6345
21. Lorensen, W., Cline, H.: Marching cubes: a high resolution 3D surface construction algorithm. In: Proceedings of 14th Annual Conference on Computer Graphics and Interactive Techniques - SIGGRAPH 1987, pp. 163–169. ACM (1987). https://doi.org/10.1145/37401.37422
22. Burt, L., Liang, Z., Sajobi, T., Hanley, D., Boyd, S.: Sex- and site-specific normative data curves for HR-pQCT. J. Bone Miner. Res. **31**(11), 2041–2047 (2016). https://doi.org/10.1002/jbmr.2873
23. Buie, H., Campbell, G., Klinck, R., MacNeil, J., Boyd, S.: Automatic segmentation of cortical and trabecular compartments based on a dual threshold technique for in vivo micro-CT bone analysis. Bone **41**(4), 505–515 (2007). https://doi.org/10.1016/j.bone.2007.07.007
24. Kameo, Y., Adachi, T.: Modeling trabecular bone adaptation to local bending load regulated by mechanosensing osteocytes. Acta Mech. **225**(10), 2833–2840 (2014). https://doi.org/10.1007/s00707-014-1202-5
25. Yang, I., Tomlin, C.: Identification of surface tension in mean curvature flow. In: Proceedings of 2013 American Control Conference, pp. 3284–3289. IEEE (2013). https://doi.org/10.1109/ACC.2013.6580338
26. Yang, I., Tomlin, C.: Regularization-based identification for level set equations. In: Proceedings of 52nd Annual Conference on Decision and Control - CDC 2013, pp. 1058–1064. IEEE (2013). https://doi.org/10.1109/CDC.2013.6760022